CORONAVIRUS

Administration of aerosolized SARS-CoV-2 to K18-hACE2 mice uncouples respiratory infection from fatal neuroinvasion

Valeria Fumagalli[1,2]†, Micol Ravà[1]†, Davide Marotta[1,2]†, Pietro Di Lucia[1], Chiara Laura[1,2,3], Eleonora Sala[1,2], Marta Grillo[1], Elisa Bono[1], Leonardo Giustini[1], Chiara Perucchini[1], Marta Mainetti[1], Alessandro Sessa[4], José M. Garcia-Manteiga[3], Lorena Donnici[5], Lara Manganaro[5], Serena Delbue[6], Vania Broccoli[4,7], Raffaele De Francesco[5,8], Patrizia D'Adamo[4,9], Mirela Kuka[1,2], Luca G. Guidotti[1,2]*, Matteo Iannacone[1,2,10]*

The development of a tractable small animal model faithfully reproducing human coronavirus disease 2019 pathogenesis would arguably meet a pressing need in biomedical research. Thus far, most investigators have used transgenic mice expressing the human ACE2 in epithelial cells (K18-hACE2 transgenic mice) that are intranasally instilled with a liquid severe acute respiratory syndrome coronavirus 2 (SARS-CoV-2) suspension under deep anesthesia. Unfortunately, this experimental approach results in disproportionate high central nervous system infection leading to fatal encephalitis, which is rarely observed in humans and severely limits this model's usefulness. Here, we describe the use of an inhalation tower system that allows exposure of unanesthetized mice to aerosolized virus under controlled conditions. Aerosol exposure of K18-hACE2 transgenic mice to SARS-CoV-2 resulted in robust viral replication in the respiratory tract, anosmia, and airway obstruction but did not lead to fatal viral neuroinvasion. When compared with intranasal inoculation, aerosol infection resulted in a more pronounced lung pathology including increased immune infiltration, fibrin deposition, and a transcriptional signature comparable to that observed in SARS-CoV-2–infected patients. This model may prove useful for studies of viral transmission, disease pathogenesis (including long-term consequences of SARS-CoV-2 infection), and therapeutic interventions.

INTRODUCTION

The coronavirus disease 2019 (COVID-19) pandemic is caused by the recently identified β-coronavirus severe acute respiratory syndrome coronavirus 2 (SARS-CoV-2) (*1*, *2*). Disease severity is variable, ranging from asymptomatic infection to multi-organ failure and death. Although SARS-CoV-2 primarily targets the respiratory system, some patients with COVID-19 can also exhibit extrarespiratory symptoms, including neurological manifestations such as loss of smell (anosmia) and taste (ageusia), headache, fatigue, memory impairment, vomiting, gait disorders, and impaired consciousness (*3*–*6*). SARS-CoV-2 can infect neurons in human brain organoids (*7*, *8*), and a few studies reported the presence of SARS-CoV-2 in olfactory sensory neurons and deeper areas within the central nervous system (CNS) in fatal COVID-19 cases (*8*–*12*). However, the neurotropism of SARS-CoV-2 and a direct role of CNS infection in the pathogenesis of neurological manifestations remain highly debated.

Despite the availability of effective vaccines against SARS-CoV-2, we still know little about COVID-19 pathogenesis. The availability of tractable animal models to mechanistically dissect virological, immunological, and pathogenetic aspects of the infection with SARS-CoV-2 and future human coronaviruses would provide major benefit. Wild-type laboratory mice are poorly susceptible to SARS-CoV-2 infection because the mouse angiotensin-converting enzyme (ACE) 2 does not act as a cellular receptor for the virus (*13*). Several transgenic mouse lineages expressing the human version of the SARS-CoV-2 receptor (hACE2) support viral replication and recapitulate certain clinical characteristics of the human infection (*13*). The most widely used model is the K18-hACE2 transgenic mouse (*14*), which expresses hACE2 predominantly in epithelial cells under the control of the cytokeratin 18 (*KRT18*) promoter (*15*). K18-hACE2 mice are typically infected by intranasally instilling liquid suspensions of SARS-CoV-2 under deep anesthesia. This results in disproportionate high CNS infection leading to fatal encephalitis (*16*–*20*), which rarely occurs in patients with COVID-19. Such viral neuroinvasion severely limits the usefulness of these mouse models, hampering studies on disease pathogenesis (including long-term consequences of SARS-CoV-2 infection) and on drug discovery. Here, we report the generation and characterization of an alternative COVID-19 platform based on controlled exposure of K18-hACE2 transgenic mice to aerosolized SARS-CoV-2.

RESULTS

Intranasal inoculation, but not aerosol exposure, of SARS-CoV-2 leads to fatal neuroinvasion

SARS-CoV-2 is mainly transmitted from person to person via respiratory droplets (*21*). In an attempt to mimic this transmission

[1]Division of Immunology, Transplantation, and Infectious Diseases, IRCCS San Raffaele Scientific Institute, 20132 Milan, Italy. [2]Vita-Salute San Raffaele University, 20132 Milan, Italy. [3]Center for Omics Sciences, IRCCS San Raffaele Scientific Institute, 20132 Milan, Italy. [4]Division of Neuroscience, IRCCS San Raffaele Scientific Institute, 20132 Milan, Italy. [5]INGM - Istituto Nazionale di Genetica Molecolare "Romeo ed Erica Invernizzi", Milan, Italy. [6]Department of Biomedical, Surgical and Dental Sciences, University of Milan, Italy. [7]National Research Council of Italy, Institute of Neuroscience, Italy. [8]Department of Pharmacological and Biomolecular Sciences (DiSFeB), University of Milan, Italy. [9]Center of Advanced Services for in-vivo testing–Animal behavior Facility, IRCCS San Raffaele Scientific Institute, 20132 Milan, Italy. [10]Experimental Imaging Centre, IRCCS San Raffaele Scientific Institute, 20132 Milan, Italy.
*Corresponding author. Email: iannacone.matteo@hsr.it (M.I.); guidotti.luca@hsr.it (L.G.G.)
†These authors contributed equally to this work.

route, we made use of a nose-only inhalation tower system that allows to expose unanesthetized mice to aerosolized virus under controlled pressure, temperature, and humidity conditions (see fig. S1, A to C, and Materials and Methods). Animals were located inside a restraint with a neck clip positioned between the base of the skull and the shoulders, thus avoiding thorax compression, keeping the airways completely unobstructed, and allowing for spontaneous breathing through the nose. K18-hACE2 transgenic mice were infected with a target dose of 1×10^5 tissue culture infectious dose 50 ($TCID_{50}$) of SARS-CoV-2 either through intranasal (IN) administration with 25 µl of diluted virus or through a 20- to 30-min exposure to aerosolized virus (AR) (Fig. 1, A and B and see Materials and Methods). Pulmonary function was measured during AR exposure using plethysmography. Frequency, tidal volume, minute volume, and accumulated volume of SARS-CoV-2–exposed mice were comparable with phosphate-buffered saline (PBS)–exposed mice (fig. S1D).

As expected (*19*, *20*), IN-infected animals exhibited significant body weight loss and a severe clinical score (see Materials and Methods for details), so that, by day 6 post infection (p.i.), ~80% of them had died and the remaining ones appeared lethargic (Fig. 1, C to E, and fig. S2). By contrast, AR-infected mice maintained stable body weight and did not show any signs of disease nor mortality, including at 20 days p.i. (Fig. 1, C to E, and figs. S2 and S3). The severe disease observed in IN-infected K18-hACE2 transgenic mice was associated with the detection of high viral RNA titers and infectious virus in the brain (Fig. 1, F to I). By contrast, neither SARS-CoV-2 RNA nor infectious virus was detected in the brain of mice exposed to aerosolized virus (Fig. 1, F to I). Immunohistochemical and immunofluorescence staining confirmed the presence of the SARS-CoV-2 nucleoprotein (N-CoV-2) in the brain of IN-infected, but not AR-infected, mice (Fig. 1, J and K). Specifically, diffuse staining for SARS-CoV-2 nucleoprotein was detected throughout the cerebrum with comparable staining in the different brain areas with the notable exception of the cerebellum, where most of its cells stained negative for viral antigens (Fig. 1K). Neurons were by far the most infected brain cells as shown by the costaining of the SARS-CoV-2 nucleoprotein with the pan-neuronal marker NeuN (~90% double-positive cells; Fig. 1L and fig. S4A). Nitric oxide has been implicated as a contributor to the host's innate defense against viral infections including those affecting the CNS (*22*). Accordingly, neurons in infected brains strongly up-regulated inducible nitric oxide synthase (iNOS) (*22*), which was undetectable in neuronal cells from control, uninfected mice (Fig. 1M). By contrast, only a minor fraction of astrocytes (~2%) and microglia (~4%) stained positive for the SARS-CoV-2 nucleoprotein (Fig. 1, N and O, and fig. S4, B and C). $Iba1^+$ myeloid cells in SARS-CoV-2–infected brains were activated as revealed by the characteristic morphology (swollen processes with reduced ramifications) and CD68 positivity (Fig. 1, P and Q). Consistent with the data on the recovery of infectious virus, viral RNA, and viral antigens, we found a significant immune cell recruitment (particularly of T cells, B cells, monocytes, and eosinophils) in the brains of IN-infected, but not AR-infected, mice (fig. S4, D and E). Together, these results demonstrate a profound viral neuroinvasion that correlates with the severe health deterioration in IN-infected mice. The high viral load and widespread viral distribution in the brain of IN-infected mice contrasts with the occasional localized detection of SARS-CoV-2 in the olfactory bulbs and/or the medulla of fatal COVID-19 cases (*10*, *23*–*27*) and caution against using this model to investigate the neurological complications of SARS-CoV-2 infection in humans.

We next investigated the potential SARS-CoV-2 entry portals to the CNS in IN-infected K18-hACE2 transgenic mice. One possibility is that the virus gains access to the CNS via the blood-brain barrier, which implies a viremic phase. However, no SARS-CoV-2 RNA was ever detected in the sera of infected mice (fig. S4, F and G), consistent with earlier reports (*18*–*20*). Alternatively, SARS-CoV-2 could enter the CNS by retrograde axonal transport upon olfactory sensory neuron infection. Indeed, and in line with previous studies (*18*–*20*), viral RNA and viral antigens were detected in the olfactory bulb of IN-infected, but not AR-infected, mice (Fig. 1, R and S, and fig. S5). Overall, the data indicate that IN, but not AR, infection of K18-hACE2 transgenic mice with SARS-CoV-2 results in lethal neuroinvasion likely via retrograde axonal transport after olfactory sensory neuron infection.

Aerosol exposure of K18-hACE2 transgenic mice to SARS-CoV-2 leads to efficient respiratory infection, anosmia, and fibrin deposition in the lung

We next analyzed viral replication in the upper respiratory tract of K18-hACE2 transgenic mice infected with SARS-CoV-2 via IN inoculation or AR exposure. We detected the presence of SARS-CoV-2 RNA in the nasal turbinates of both AR- and IN-infected mice at days 3 and 6 p.i. (Fig. 2, A and B). To examine whether viral replication within the upper respiratory tract induced anosmia, we subjected AR- and IN-infected mice to a social scent discrimination assay (Fig. 2C) (*19*). If olfaction is normal (as in PBS-treated controls), then male mice exposed to tubes containing male or female bedding preferentially spend time sniffing the female scent (Fig. 2, D to F). By contrast, both AR- and IN-infected mice spent significantly less time sniffing the female scent at day 3 p.i. (Fig. 2, D and E), indicative of hyposmia or anosmia. At day 3 p.i., the mobility of both AR- and IN-infected mice was normal, as there were no differences in the amount of time spent sniffing the male tube (Fig. 2D). At day 6 p.i., AR-infected mice still showed signs of hyposmia/anosmia, whereas IN-infected mice were completely lethargic preventing further analyses (Fig. 2, D to F). The data obtained in AR-infected mice are consistent with the hypothesis that hyposmia or anosmia occurs because of the infection of olfactory epithelium and in the absence of CNS infection or general malaise (*19*, *28*, *29*).

We next assessed viral replication in the lower respiratory tract of SARS-CoV-2–infected K18-hACE2 transgenic mice. We detected comparable amounts of SARS-CoV-2 RNA and infectious virus from the lungs of mice infected with the two different routes of administration at both days 3 and 6 p.i. (Fig. 2, G to J). Immunohistochemical and immunofluorescence staining for the SARS-CoV-2 nucleoprotein confirmed similar levels of viral antigens and similar staining patterns in the lungs of IN- and AR-infected mice (Fig. 2K). To gain insight into the impact of infection on lung physiology, pulmonary function was measured at days 3 and 5 p.i. via whole-body plethysmography (WBP). Consistent with previously published data (*30*, *31*), we confirmed that, when compared with control mice, IN-infected mice exhibited a significant loss in pulmonary function as indicated by changes in, e.g., respiratory frequency, tidal volume, Rpef (a measure of airway obstruction), and PenH [a controversial metric that has been used by some as an indirect measure of airway resistance and by others as a nonspecific assessment of breathing

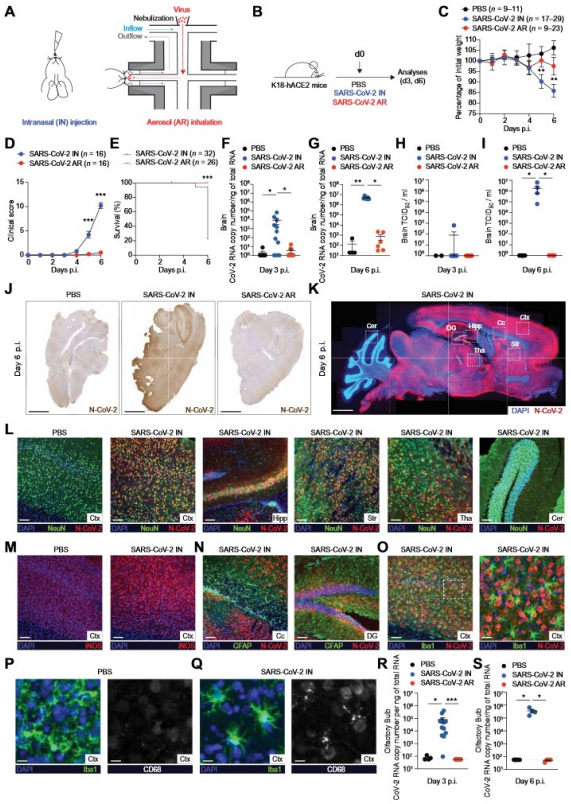

Fig. 1. Intranasal inoculation, but not AR, of SARS-CoV-2 leads to fatal neuroinvasion in K18-hACE2 transgenic mice. (**A**) Illustration of the two modalities used to infect K18-hACE2 mice with SARS-CoV-2. On the left, IN injection is shown. On the right, representation of an unanesthetized mouse placed in the nose-only Allay restrainer on the inhalation chamber is shown. In red, AR with a particle size of ~4 μm; in light-blue, primary flow set to 0.5 liter/min per port; in gray, mouse breathing outflow (see Materials and Methods). (**B**) Schematic representation of the experimental setup. K18-hACE2 mice were infected with a target dose of 1×10^5 $TCID_{50}$ of SARS-CoV-2 through IN administration or through AR exposure. Lung, brain, nasal turbinates, olfactory bulbs, and blood were collected and analyzed 3 and 6 days p.i. (**C**) Mouse body weight was monitored daily for up to 6 days and is expressed as the percentage of weight relative to the initial weight on day 0. Statistical significance of comparison between IN-infected ($n = 17$ to 29, blue dots) and AR-infected mice ($n = 9$ to 23, red dots) is shown. Control mice treated with PBS are also shown ($n = 9$ to 11, black dots). Data are represented as means ± SEM. *n* indicate a range of mice, some of them have been dropped out from the analysis to be sacrificed for planned experimental end points. (**D**) Clinical score was assessed evaluating the piloerection (0 to 3), posture (0 to 3), activity level (0 to 3), eye closure (0 to 3), and breathing (0 to 3) (see Materials and Methods). Statistical significance of comparison between IN-infected ($n = 16$, blue dots) and AR-infected mice ($n = 16$, red dots) is shown. PBS-treated control mice did not exhibit any clinical signs. (**E**) Survival curve of IN-infected ($n = 32$, blue dots) and AR-infected mice ($n = 26$, red dots). (**F** and **G**) Quantification of SARS-CoV-2 RNA in the brain of IN-infected ($n = 7$ to 11, blue dots) and AR-infected ($n = 6$ to 10, red dots) mice and of PBS-treated control mice ($n = 4$, black dots) measured 3 days (F) and 6 days (G) p.i. RNA values are expressed as copy number per nanogram of total RNA, and the limit of detection is indicated as a dotted line. (**H** and **I**) Viral titers in the brain were determined 3 (H) and 6 days (I) p.i. by $TCID_{50}$. PBS-treated control mice: $n = 2$ to 3, black dots; IN-infected mice: $n = 4$, blue dots; AR-infected mice: $n = 4$, red dots. (**J**) Representative immunohistochemical micrographs of sagittal brain sections from PBS-treated control mice (left), IN-infected mice (middle), and AR-infected mice (right) 6 days p.i. N-SARS-CoV-2–positive cells are depicted in brown. Scale bars, 1 mm. (**K**) Representative confocal immunofluorescence staining for N-CoV-2 (red) in sagittal brain sections of IN-infected mice. Cell nuclei are depicted in blue. White boxes indicate different brain areas: cerebellum (Cer), dentate gyrus (DG), hippocampus (Hipp), corpus callosum (Cc), cerebral cortex (Ctx), thalamus (Tha), and striatum (Str). Scale bar, 1 mm. (**L**) Representative confocal immunofluorescence micrographs of sagittal brain sections from PBS-treated control mice (first panel) and IN-infected mice 6 days p.i. N-CoV-2 is depicted in red, NeuN neural marker is depicted in green, and cell nuclei are depicted in blue. Fields of cerebral cortex, hippocampus, striatum, thalamus, and cerebellum are shown. Scale bars, 100 μm. (**M**) Representative confocal immunofluorescence micrographs of cerebral cortex in PBS-treated control mice (left) and IN-infected mice (right) 6 days p.i. $iNOS^+$ cells are depicted in red and cell nuclei in blue. Scale bars, 100 μm. (**N**) Representative confocal immunofluorescence micrographs of two areas of the brain from IN-infected mice 6 days p.i. Corpus callosum of the cerebral cortex (left) and dentate gyrus (right). N-CoV-2 is depicted in red, glial fibrillary acidic protein astroglial marker is depicted in green, and cell nuclei are depicted in blue. Scale bars, 100 μm. (**O**) Representative confocal immunofluorescence micrographs of the cerebral cortex of IN-infected mice at 6 days p.i. N-CoV-2 is depicted in red, Iba1 microglial marker is depicted in green, and cell nuclei are depicted in blue. White box indicates the magnification represented in the right panel. Scale bars, 100 μm (image) and 25 μm (magnification). (**P** and **Q**) Representative confocal immunofluorescence micrographs of the cerebral cortex of PBS-treated control mice (P) and IN-infected mice (Q) 6 days p.i. Left panels show Iba1 microglial marker in green and cell nuclei in blue; right panel shows CD68 marker of microglial activation in white. Scale bars, 10 μm. (**R** and **S**) Quantification of SARS-CoV-2 RNA in the olfactory bulbs of IN-infected ($n = 4$ to 12, blue dots) and AR-infected ($n = 4$ to 12, red dots) mice and of PBS-treated control mice ($n = 2$ to 4, black dots) measured 3 days (R) and 6 days (S) p.i. RNA values are expressed as copy number per nanogram of total RNA, and the limit of detection is indicated as a dotted line. Data are expressed as means ± SEM. Data in (C) to (I), (R), and (S) are pooled from two independent experiments per time point. *$P < 0.05$, **$P < 0.01$, and ***$P < 0.001$; two-way ANOVA followed by Sidak's multiple comparison test (C and D, comparison between blue and red dots for each time point); Log-rank (Mantel-Cox) test (E); Kruskal-Wallis test (F to I, R, and S).

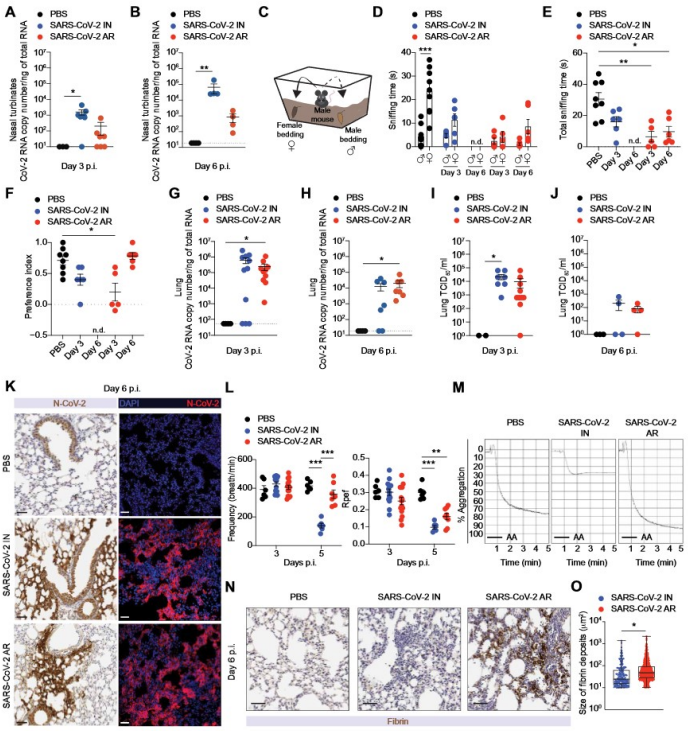

Fig. 2. AR of K18-hACE2 transgenic mice to SARS-CoV-2 leads to efficient respiratory infection, anosmia, and fibrin deposition in the lung. (**A** and **B**) Quantification of SARS-CoV-2 RNA in the nasal turbinates of PBS-treated control mice ($n = 3$, black dots) and of IN-infected ($n = 4$ to 7, blue dots) and AR-infected ($n = 4$ to 7, red dots) mice 3 days (A) and 6 days (B) p.i. RNA values are expressed as copy number per nanogram of total RNA, and the limit of detection is indicated as a dotted line. (**C**) Illustration showing social scent discrimination test. Male mice were free to investigate for 5 min with two different tubes containing their own cage bedding or female cage bedding placed at two opposite corners of a clean cage. (**D** and **E**) Time that males spent sniffing their own male scent or female scent (D) and the sum of the two times (E) are expressed as time sniffing (s). Analyses were performed 3 or 6 days after IN ($n = 3$ to 6, blue dots) or AR infection ($n = 3$ to 5, red dots). As control, PBS-treated mice are shown ($n = 8$, black dots). In (D), comparison between female and male time in each group of mice. n.d., the sniffing time could not be determined because mice were completely lethargic. (**F**) Preference index for male mice was calculated as (female time − male time) / (total sniffing time female + male), as an indicator of the time spent sniffing preferred (female) or nonpreferred (male) scents. n.d., the sniffing time could not be determined because mice were completely lethargic. (**G** and **H**) Quantification of SARS-CoV-2 RNA in the lungs of IN-infected ($n = 7$ to 11, blue dots) and AR-infected ($n = 7$ to 10, red dots) mice and of PBS-treated control mice ($n = 4$, black dots) measured 3 days (G) and 6 days (H) p.i. RNA values are expressed as copy number per nanogram of total RNA, and the limit of detection is indicated as a dotted line. (**I** and **J**) Viral titers in the lungs were determined 3 (I) and 6 days (J) p.i. by $TCID_{50}$. PBS-treated control mice: $n = 2$ to 3, black dots; IN-infected mice: $n = 4$ to 7, blue dots; AR-infected mice: $n = 4$ to 10, red dots. (**K**) Representative immunohistochemical (left) and confocal immunofluorescence (right) micrographs of lung sections from PBS-treated control mice (top), IN-infected mice (middle), and AR-infected mice (bottom) at 6 days p.i. N-CoV-2–positive cells are depicted in brown (left) or in red (right). Cell nuclei are depicted in blue (right). Scale bars, 30 µm. (**L**) Pulmonary function was assessed by WBP performed 3 and 5 days after IN ($n = 6$ to 14, blue dots) and AR infection ($n = 7$ to 14, red dots). As control, PBS-treated mice were evaluated ($n = 6$, black dots). Frequency (left) and Rpef (right) parameters are shown. Calculated respiratory values were averaged over a 15-min data collection period. (**M**) Representative aggregometry curves induced by arachidonic acid (AA) on platelet-rich plasma from PBS-treated control mice (left), IN-infected mice (middle), and AR-infected mice (right) 6 days p.i. Platelet aggregation was measured by light transmission aggregometry for 5 min and is expressed as % aggregation. (**N**) Representative immunohistochemical micrographs of lung sections from PBS-treated control mice (left), IN- (middle), and AR-infected mice (right) at 6 days p.i. Fibrin deposition is shown in brown. Scale bars, 30 µm. (**O**) Quantification of the size of fibrin deposits (μm^2). $n = 4$. Data are expressed as means ± SEM and are pooled from two independent experiments per time point. *$P < 0.05$, **$P < 0.01$, and ***$P < 0.001$, Kruskal-Wallis test (A, B, and E to J), two-way ANOVA followed by Sidak's multiple comparison test (L), and Mann-Whitney *U* test two-tailed (D and O). In (D), statistical analysis was performed comparing female and male sniffing time within the same experimental group of mice.

patterns (*31*–*34*)] (Fig. 2L and fig. S6A). Most of these respiratory parameters were normal or much less altered in AR-infected mice, suggesting that the observed changes in IN-infected mice were mostly due to CNS infection. One notable exception is Rpef, a calculated index of airway resistance that considers the time needed to reach maximum expiratory flow and the total expiratory time (*31*). Rpef was the only metric that was consistently altered in AR-infected mice (and to the same extent as in IN-infected mice), suggesting that this

index might truly reflect lung infection and pathology, rather than CNS involvement.

COVID-19, particularly in its most severe forms, has been associated with thrombotic phenomena that entail increased platelet activation and aggregation, and fibrin deposition in the lungs (*35*–*39*). We therefore set out to assess platelet function by performing light transmission aggregometry of platelet-rich plasma (PRP) obtained from infected mice. Whereas IN infection resulted in an impaired platelet aggregation, PRP from AR-infected mice showed a normal or even increased aggregation (Fig. 2M). This was associated with increased fibrin deposition and larger platelet aggregates in the lungs of AR-infected mice (Fig. 2, N and O, and fig. S6B). Together, the data indicate that AR exposure of K18-hACE2 transgenic mice to SARS-CoV-2 results in robust viral replication in the respiratory tract, anosmia, airway obstruction, and platelet aggregation with fibrin deposition in the lung.

Although the vigorous SARS-CoV-2 replication in the lungs of AR-infected K18-hACE2 transgenic mice suggests that these mice de facto inhaled at least the same amount of virus as IN-infected mice, it is theoretically possible that a higher viral inoculum would have resulted in fatal neuroinvasion even upon AR delivery. To further increase viral replication in the infected hosts, we transiently inhibited type 1 interferon (IFN) receptor signaling with anti-IFNAR1 blocking antibodies (Abs) before AR infection (fig. S7A). As expected, higher levels of viral RNA (fig. S7B) and infectious virus (fig. S7C) were detected in the lungs of mice treated with anti-IFNAR1 Abs compared with control mice. The presence of higher amounts of virus in the lungs of anti-IFNAR1–treated mice was confirmed by immunohistochemical staining for the SARS-CoV-2 nucleoprotein (fig. S7D). Despite the increased lung viral load, we failed to detect SARS-CoV-2 RNA, infectious virus, or viral antigens in the brain of anti-IFNAR1–treated AR-infected mice (fig. S7, E to G).

Histopathological changes, immune response, and transcriptional signatures in the lungs of infected mice

We next sought to better characterize the histopathological changes and the immune response in the lungs of SARS-CoV-2–infected mice. Hematoxylin and eosin (H&E) staining revealed an inflammatory process that peaked at day 6 p.i. and appeared more severe in AR- than in IN-infected mice (Fig. 3A and fig. S8A). Lung sections revealed interstitial edema, consolidation, alveolar wall thickening, and immune infiltration of both polymorphonuclear and mononuclear cells in the alveolar and the interstitial space (Fig. 3A and fig. S8A). Consistent with the histology, the absolute number of cells recovered 6 days p.i. from the lungs and bronchoalveolar lavage (BAL) was significantly higher in AR-infected than in IN-infected mice (Fig. 3, B to E). Specifically, the differences in immune cell recruitment could be attributed to an increase in $CD4^+$ and $CD8^+$ T cells and in monocytes (Fig. 3, B to E). A higher number of TCR-β^+ T cells in the lung of AR-infected mice was confirmed by confocal immunofluorescence histology (fig. S8B).

Next, we sought to analyze the transcriptome in the lungs of infected K18-hACE2 mice by performing bulk RNA sequencing (RNA-seq) of lung homogenates 6 days after SARS-CoV-2 infection. Principal components analysis revealed distinct transcriptional signatures between AR-infected, IN-infected, and uninfected mice (Fig. 3F). Genes up-regulated upon AR infection were associated to adaptive immune responses and to immune system signaling by IFNs and other cytokines (Fig. 3G, fig. S9, and data file S1). In particular, the transcription of genes related to cytokine-mediated signaling, type I IFN signaling, and cellular response to IFN-γ (*18*) was increased in the lungs of AR-infected mice with respect to IN-infected ones (Fig. 3, H and I, and data file S1). Many human orthologs of the genes up-regulated in the lungs of AR-infected mice were found to be also induced in patients with COVID-19, including genes related to leukocyte trafficking (e.g., *Ccl11*, *Ccl8*, *Ccl2*, *Cxcl9*, and *Cxcl10*), antiviral response induced by type I IFN (*Ifitm3*, *Ifit2*, *Oas1a*, *Oas3*, *Stat1*, *Irf1*, *Mx1*, *Mx2*, and *Isg15*), and tumor necrosis factor (TNF) (*Tnfsf10*) (*40*–*42*)(Fig. 3I, fig. S9, and data file S1). *Ccl8* and *Ccl2* as well as *Cxcl9* and *Cxcl10*, chemoattractants for monocytes and T cells, respectively, were significantly up-regulated in the lungs of AR-infected mice and in patients with COVID-19 (*40*–*42*), in line with the increased recruitment of these cells (Fig. 3I, fig. S9C, and data file S1). The enrichment of the gene signature related to the cellular response to IFN-γ in AR-infected mice prompted us to assess SARS-CoV-2–specific T cell responses. Antigen-specific $CD8^+$ and $CD4^+$ T cells recovered from lung homogenates were assessed for IFN-γ, TNF-α, and Granzyme B (Gz-B) expression upon in vitro stimulation with the H2-D^b–restricted S538-546 and I-A^b–restricted ORF3a 266-280 immunodominant peptides (*43*). In line with the RNA-seq data, we found that the absolute number of IFN-γ^+ TNF-α^+ virus-specific $CD8^+$ and $CD4^+$ T cells were significantly higher in the lungs of AR-infected mice compared with IN-infected mice (Fig. 3, J and K). Together, our data show that, when compared with IN inoculation, AR infection resulted in a more pronounced lung pathology including increased immune infiltration and, in a transcriptional signature, comparable with that observed in SARS-CoV-2–infected patients.

DISCUSSION

We have generated and characterized an alternative COVID-19 platform based on controlled AR exposure of K18-hACE2 transgenic mice to SARS-CoV-2. Mice infected via AR develop robust respiratory infection, anosmia, and signs of airway obstruction but, in contrast to mice infected intranasally, do not experience fatal neuroinvasion. Moreover, when compared with IN inoculation, AR exposure results in a more severe lung pathology, inflammation, and fibrin deposition.

The observation that mice infected via AR exposure develop anosmia in the absence of neuroinvasion is of interest in light of the notion that olfactory dysfunction is a strong and consistent symptom associated with a positive COVID-19 test in humans (*44*). The pathophysiology of anosmia triggered by SARS-CoV-2 remains unclear. However, our results, as well as previously published studies (*19*, *28*, *29*, *45*–*47*), support the hypothesis that anosmia stems from infection of sustentacular cells and/or Bowman's glands rather than of olfactory sensory neurons. Sustentacular cells and Bowman's glands in both K18-hACE2 transgenic mice and humans express high levels of the SARS-CoV-2 receptor ACE2 and the internalization enhancer TMPRSS2 (*47*). Infected sustentacular cells and/or Bowman's glands may, in turn, produce proinflammatory cytokines affecting olfactory sensory neurons (*29*, *48*). Alternatively, damaged sustentacular cells and/or Bowman's glands may lead to an overall disorganization of the olfactory epithelium, ultimately leading to defective signal transduction to the olfactory bulb (*49*–*51*). Elucidation of the molecular mechanisms underlying anosmia during COVID-19 will require further studies.

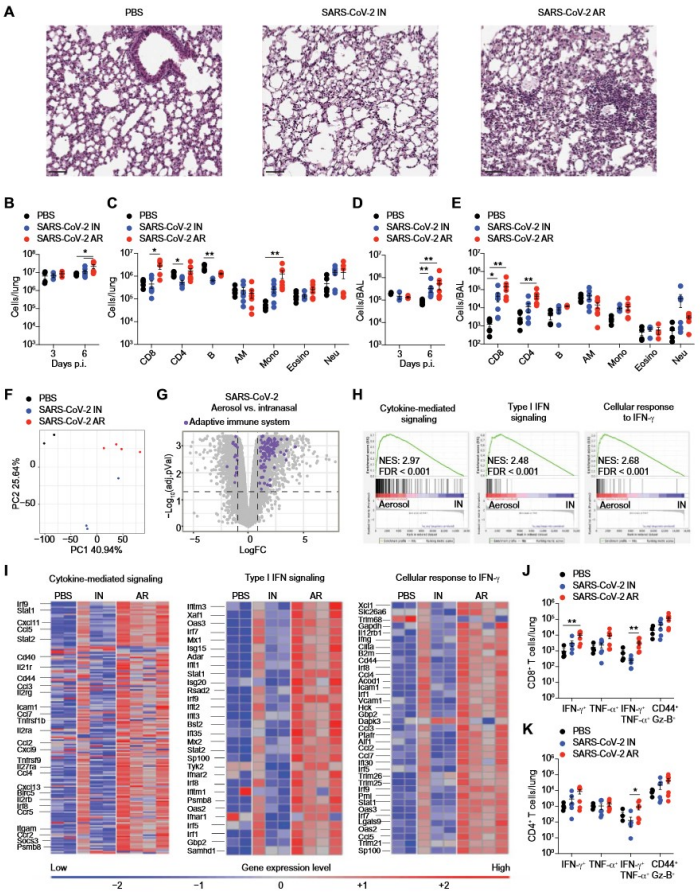

Fig. 3. Histopathological changes, immune response, and transcriptional signatures in the lungs of infected mice. (**A**) Representative H&E micrographs of lung sections from PBS-treated control mice (left), IN-infected mice (middle), and AR-infected mice (right) 6 days p.i. Scale bars, 50 μm. (**B** to **E**) Absolute number of total cells (B and D) and of single-cell populations (C and E) recovered from lung homogenates (B and C) and BAL (D and E) of PBS-treated control mice ($n = 4$ to 6, black dots), IN-infected mice ($n = 3$ to 7, blue dots), and AR-infected mice ($n = 3$ to 7, red dots) analyzed 6 days p.i. $CD8^+$ T cells (Live, $CD45^+$, $CD8^+$); $CD4^+$ T cells (Live, $CD45^+$, $CD4^+$); B cells (Live, $CD45^+$, $CD8^-$, $CD4^-$, $B220^+$, $CD19^+$); AM, alveolar macrophages (Live, $CD45^+$, $CD8^-$, $CD4^-$, $Ly6g^-$, $CD11b^-$, $F4/80^+$, $SiglecF^{hi}$); Mono, monocytes (Live, $CD45^+$, $CD8^-$, $CD4^-$, $Ly6g^-$, $SiglecF^-$, $CD11b^+$, $Ly\text{-}6c^+$); Eosino, eosinophils (Live, $CD45^+$, $CD8^-$, $CD4^-$, $Ly6g^-$, $CD11b^+$, $SiglecF^{int}$); Neu, neutrophils (Live, $CD45^+$, $CD8^-$, $CD4^-$, $CD11b^+$, $Ly6g^+$). (**F**) Principal components (PC) analysis (PCA) of RNA-seq expression values from the lungs of PBS-treated, control ($n = 2$, black), IN-infected mice ($n = 3$, blue), and AR-infected ($n = 4$, red) mice. Percentages indicate the variance explained by each PC. (**G**) Volcano plot of RNA-seq results. The *x* axis represents the log2 fold change (FC) of differentially expressed genes (DEG) comparing AR to IN infection, and the *y* axis represents the $-\log_{10}$(false discovery rate). Genes significantly up-regulated in AR- relative to IN-infected mice ($|\log FC| > 1$ and adjusted $P < 0.05$, horizontal and vertical dashed line) belonging to the "Adaptive immune system" pathway from BioPlanet 2019 (*55*) are highlighted in violet. (**H**) Gene set enrichment analysis of three gene sets described in (*18*), comparing the transcriptome of IN- and AR-infected mice, presented as the running enrichment score for the gene set as the analysis "walks down" the ranked list of genes (reflective of the degree to which the gene set is over-represented at the top or bottom of the ranked list of genes) (top), the position of the gene set members (black vertical lines) in the ranked list of genes (middle), and the value of the ranking metric (bottom). NES, normalized enrichment score. (**I**) Heatmaps of genes (one per row) belonging to the three signatures as in (H), expressed in logarithmic normalized read counts. Each column represents an individual sample. (**J** and **K**) Absolute number of $CD8^+$ (J) and $CD4^+$ (K) T cells producing IFN-γ, TNF-α, or both and expressing CD44 and Gz-B in the lungs of PBS-treated control mice ($n = 4$, black dots), IN-infected mice ($n = 5$, blue dots), and AR-infected mice ($n = 5$, red dots) 6 days p.i.. Data are expressed as means ± SEM. Data in (B) to (E), (J), and (K) are pooled from two independent experiments. $^*P < 0.05$ and $^{**}P < 0.01$, Kruskal-Wallis test (B to E, J, and K).

The difference in immune infiltration in the lungs between IN and AR infection (despite similar viral loads) remains poorly understood. A possible explanation lies in CNS injury causing immune deficiency (*52*). Similarly, the observed failure of platelet aggregation might be influenced by CNS damage (*53*). Previous studies have looked at how the route of inoculation affects the immune response and disease outcome upon viral infection. For instance, one study directly compared IN instillation with AR inoculation of mice with influenza virus and concluded that AR delivery resulted in a more robust infection, pulmonary cell infiltration and inflammation, and morbidity (*54*). We believe that this model may allow studies on viral transmission (e.g., by analyzing the effect of aerosol particle size, humidity, and temperature on infectivity), on disease pathogenesis (including, potentially, thrombotic events and long-term consequences of infection), and on therapeutic interventions.

MATERIALS AND METHODS

Please see Supplementary Methods for additional details.

Study design

The aim of this study was to develop mouse models of COVID-19 pathogenesis and treatment. We used SARS-CoV-2/human/ITA/Milan-UNIMI-1/2020 as virus, K18-hACE2 transgenic mice as model organism, and a nose-only inhalation tower system to expose mice to aerosolized virus under controlled conditions. Mouse experiments were planned in accordance with the principles of the 3Rs (replacement, reduction, and refinement). Body weight, morbidity, and mortality were recorded. Olfactory and respiratory functions were measured by social scent discrimination assay and by WBP, respectively. Viral content in different organs was measured by $TCID_{50}$, by quantitative polymerase chain reaction (qPCR), by immunohistochemistry, and by immunofluorescence. Immune infiltrate and pathological changes were examined in different organs by flow cytometry and by histology/immunohistochemistry, respectively. Platelet function was measured via light aggregometry and fibrin deposition by immunohistochemistry. Gene expression was analyzed by qPCR and RNA-seq. Sample size and replicates for each experiment are indicated in figure legends. During analysis, no individual data points were excluded under any circumstances other than technical failure to process the sample. Animals were randomized to the experimental groups.

Mice

B6.Cg-Tg(K18-ACE2)^{2Prlmn}/J mice (referred to in the text as K18-hACE2) were purchased from the Jackson Laboratory. Mice were housed under specific pathogen–free conditions, and heterozygous mice of both sexes were used at 8 to 10 weeks of age. All experimental animal procedures were approved by the Institutional Animal Committee of the San Raffaele Scientific Institute, and all infectious work was performed in designed biosafety level 3 (BSL-3) workspaces.

Virus

The SARS-CoV-2/human/ITA/Milan-UNIMI-1/2020 (GenBank: MT748758.1) isolation was carried out in BSL-3 workspace and performed in Vero E6 cells, which were cultured at 37°C and 5% CO2 in complete medium [Dulbecco's modified Eagle's medium supplemented with 10% fetal bovine serum, MEM nonessential amino acids, penicillin (100 U/ml), streptomycin (100 U/ml), and 2 mM L-glutamine]. Virus stocks were titrated using Endpoint Dilution Assay (TCID50/ml). Vero E6 cells were seeded into 96-well plates and infected at 95% of confluency with base 10 dilutions of virus stock. After 1 hour of adsorption at 37°C, the cell-free virus was removed, cells were washed with PBS 1×, and complete medium was added to cells. After 48 hours, plates were evaluated for the presence of a cytopathic effect. TCID50 per milliliter of viral stocks were then determined by applying the Reed-Muench formula.

Nose-only inhalation tower system

The Data Sciences International (DSI) nose-only inhalation tower system (DSI Buxco respiratory solutions, DSI) is composed of seven open ports where mice are exposed to aerosolized virus. Mice were placed in the DSI Allay restraint. The Allay collar is positioned between the base of the mouse skull and its shoulders, thus avoiding thorax compression and maintaining normal breathing patterns. Liquid virus was aerosolized by an Aeroneb (Aerogen) vibrating mesh nebulizer that generates particles of ~4-μm in size that were uniformly delivered to all the tower ports. One port of the tower was occupied by a temperature and humidity probe for real-time monitoring of the tower conditions. The inhalation tower controller software was used to define the flow and pressure of the inhalation tower and the temperature, humidity, and the ratio O_2/CO_2 inside the tower. During virus exposure, mice were monitored through plethysmography for frequency, tidal volume, minute volume, and accumulated volume. The whole system was placed inside a class II biological safety hood that is located in a BSL-3 facility.

Mouse infection through aerosol exposure (AR) or IN administration

Unanesthetized K18-hACE2 mice were placed in a nose-only Allay restrainer on the inhalation chamber (DSI Buxco respiratory solutions, DSI). To reach a target accumulated inhaled aerosol (also known as delivered dose) of 1×10^5 TCID50, mice were exposed to aerosolized SARS-CoV-2 for 20 to 30 min (depending on the total volume of diluted virus and on the number of mice simultaneously exposed). Primary inflows and pressure were controlled and set to 0.5 liter/min per port and −0.5 cmH_2O, respectively. As control, K18-hACE2 mice received the same volume of aerosolized PBS (125 μl per mouse). Intranasal administration of 1×10^5 TCID50 of SARS-COV-2 per mouse in a total volume of 25 μl of PBS was performed under 2% isoflurane (#Iso-Vet 250) anesthesia. Infected mice were monitored daily to record body weight and clinical and respiratory parameters. The clinical score was based on a cumulative 0 to 3 scale evaluating fur, posture, activity level, eyes, and breathing (see table S1).

Social scent discrimination test

The social scent discrimination test was used to assess hyposmia/anosmia in IN-infected or AR-infected male mice compared with PBS-treated control male mice, as previously described (*19*). Briefly, two 2-ml Eppendorf tubes containing beddings from the cage of grouped females and from the experimental male were placed at two opposing corners of a clean cage. Experimental male mice were scored for 5 min for the time spent in sniffing the tubes, considering only the time when the nose was inside one of the two tubes. Control male mice preferentially explored the tube containing the female bedding. Preference index was calculated as: (time spent to sniff

female tube − time spent to sniff male tube) / (time spent to sniff female tube + time spent to sniff male tube).

Whole-body plethysmography

WBP was performed using WBP chamber (DSI Buxco respiratory solutions, DSI). Mice were allowed to acclimate inside the chamber for 10 min before recording respiratory parameters for 15 min using the FinePointe software.

Statistical analyses and software

Detailed information concerning the statistical methods used is provided in the figure legends. Flow and imaging data were collected using FlowJo version 10.5.3 (Treestar) and Imaris (Bitplane), respectively. Statistical analyses were performed with GraphPad Prism software version 8 (GraphPad). Immunohistochemical imaging quantifications were performed with QuPath (Quantitative Pathology & Bioimage 5 Analysis) software. n represents individual mice analyzed per experiment. Experiments were performed independently at least twice to control for experimental variation. Error bars indicate the SEM. We used Mann-Whitney U tests to compare two groups with non-normally distributed continuous variables and Kruskal-Wallis nonparametric test to compare three or more unpaired groups. We used two-way analysis of variance (ANOVA) followed by Sidak's multiple comparisons tests to analyze experiments with multiple groups and two independent variables. Kaplan-Meier curves were compared with the Log-rank (Mantel-Cox) test. Significance is indicated as follows: $^{*}P < 0.05$, $^{**}P < 0.01$, and $^{***}P < 0.001$. Comparisons are not statistically significant unless indicated.

SUPPLEMENTARY MATERIALS

www.science.org/doi/10.1126/sciimmunol.abl9929
Methods
Figs. S1 to S9
Tables S1 and S2
Data files S1 and S2
References (*56*–*65*)

View/request a protocol for this paper from *Bio-protocol*.

REFERENCES AND NOTES

1. F. Wu, S. Zhao, B. Yu, Y.-M. Chen, W. Wang, Z.-G. Song, Y. Hu, Z.-W. Tao, J.-H. Tian, Y.-Y. Pei, M.-L. Yuan, Y.-L. Zhang, F.-H. Dai, Y. Liu, Q.-M. Wang, J.-J. Zheng, L. Xu, E. C. Holmes, Y.-Z. Zhang, A new coronavirus associated with human respiratory disease in China. *Nature* **579**, 265–269 (2020).
2. P. Zhou, X.-L. Yang, X.-G. Wang, B. Hu, L. Zhang, W. Zhang, H.-R. Si, Y. Zhu, B. Li, C.-L. Huang, H.-D. Chen, J. Chen, Y. Luo, H. Guo, R.-D. Jiang, M.-Q. Liu, Y. Chen, X.-R. Shen, X. Wang, X.-S. Zheng, K. Zhao, Q.-J. Chen, F. Deng, L.-L. Liu, B. Yan, F.-X. Zhan, Y.-Y. Wang, G.-F. Xiao, Z.-L. Shi, A pneumonia outbreak associated with a new coronavirus of probable bat origin. *Nature* **579**, 270–273 (2020).
3. J. Helms, S. Kremer, H. Merdji, R. Clere-Jehl, M. Schenck, C. Kummerlen, O. Collange, C. Boulay, S. Fafi-Kremer, M. Ohana, M. Anheim, F. Meziani, Neurologic features in severe SARS-CoV-2 infection. *N. Engl. J. Med.* **382**, 2268–2270 (2020).
4. C. Qiu, C. Cui, C. Hautefort, A. Haehner, J. Zhao, Q. Yao, H. Zeng, E. J. Nisenbaum, L. Liu, Y. Zhao, D. Zhang, C. G. Levine, I. Cejas, Q. Dai, M. Zeng, P. Herman, C. Jourdaine, K. de With, J. Draf, B. Chen, D. T. Jayaweera, J. C. Denneny, R. Casiano, H. Yu, A. A. Eshraghi, T. Hummel, X. Liu, Y. Shu, H. Lu, Olfactory and gustatory dysfunction as an early identifier of COVID-19 in adults and children: An international multicenter study. *Otolaryngol. Head Neck Surg.* **163**, 714–721 (2020).
5. M. S. Xydakis, P. Dehgani-Mobaraki, E. H. Holbrook, U. W. Geisthoff, C. Bauer, C. Hautefort, P. Herman, G. T. Manley, D. M. Lyon, C. Hopkins, Smell and taste dysfunction in patients with COVID-19. *Lancet Infect. Dis.* **20**, 1015–1016 (2020).
6. C. Iadecola, J. Anrather, H. Kamel, Effects of COVID-19 on the nervous system. *Cell* **183**, 16–27.e1 (2020).
7. A. Ramani, L. Müller, P. N. Ostermann, E. Gabriel, P. Abida-Islam, A. Müller-Schiffmann, A. Mariappan, O. Goureau, H. Gruell, A. Walker, M. Andrée, S. Hauka, T. Houwaart, A. Dilthey, K. Wohlgemuth, H. Omran, F. Klein, D. Wieczorek, O. Adams, J. Timm, C. Korth, H. Schaal, J. Gopalakrishnan, SARS-CoV-2 targets neurons of 3D human brain organoids. *EMBO J.* **39**, e106230 (2020).
8. E. Song, C. Zhang, B. Israelow, A. Lu-Culligan, A. V. Prado, S. Skriabine, P. Lu, O.-E. Weizman, F. Liu, Y. Dai, K. Szigeti-Buck, Y. Yasumoto, G. Wang, C. Castaldi, J. Heltke, E. Ng, J. Wheeler, M. M. Alfajaro, E. Levavasseur, B. Fontes, N. G. Ravindra, D. V. Dijk, S. Mane, M. Gunel, A. Ring, S. A. J. Kazmi, K. Zhang, C. B. Wilen, T. L. Horvath, I. Plu, S. Haik, J.-L. Thomas, A. Louvi, S. F. Farhadian, A. Huttner, D. Seilhean, N. Renier, K. Bilguvar, A. Iwasaki, Neuroinvasion of SARS-CoV-2 in human and mouse brain. *J. Exp. Med.* **218**, e20202135 (2021).
9. M. Glatzel, C. Hagel, J. Matschke, J. Sperhake, N. Deigendesch, A. Tzankov, S. Frank, Neuropathology associated with SARS-CoV-2 infection. *Lancet* **397**, 276 (2021).
10. J. Matschke, M. Lütgehetmann, C. Hagel, J. P. Sperhake, A. S. Schröder, C. Edler, H. Mushumba, A. Fitzek, L. Allweiss, M. Dandri, M. Dottermusch, A. Heinemann, S. Pfefferle, M. Schwabenland, D. S. Magruder, S. Bonn, M. Prinz, C. Gerloff, K. Püschel, S. Krasemann, M. Aepfelbacher, M. Glatzel, Neuropathology of patients with COVID-19 in Germany: A post-mortem case series. *Lancet Neurol.* **19**, 919–929 (2020).
11. V. G. Puelles, M. Lütgehetmann, M. T. Lindenmeyer, J. P. Sperhake, M. N. Wong, L. Allweiss, S. Chilla, A. Heinemann, N. Wanner, S. Liu, F. Braun, S. Lu, S. Pfefferle, A. S. Schröder, C. Edler, O. Gross, M. Glatzel, D. Wichmann, T. Wiech, S. Kluge, K. Pueschel, M. Aepfelbacher, T. B. Huber, Multiorgan and renal tropism of SARS-CoV-2. *N. Engl. J. Med.* **383**, 590–592 (2020).
12. G. D. de Melo, F. Lazarini, S. Levallois, C. Hautefort, V. Michel, F. Larrous, B. Verillaud, C. Aparicio, S. Wagner, G. Gheusi, L. Kergoat, E. Kornobis, F. Donati, T. Cokelaer, R. Hervochon, Y. Madec, E. Roze, D. Salmon, H. Bourhy, M. Lecuit, P.-M. Lledo, COVID-19–related anosmia is associated with viral persistence and inflammation in human olfactory epithelium and brain infection in hamsters. *Sci. Transl. Med.* **13**, eabf8396 (2021).
13. C. Muñoz-Fontela, W. E. Dowling, S. G. P. Funnell, P.-S. Gsell, A. X. Riveros-Balta, R. A. Albrecht, H. Andersen, R. S. Baric, M. W. Carroll, M. Cavaleri, C. Qin, I. Crozier, K. Dallmeier, L. de Waal, E. de Wit, L. Delang, E. Dohm, W. P. Duprex, D. Falzarano, C. L. Finch, M. B. Frieman, B. S. Graham, L. E. Gralinski, K. Guilfoyle, B. L. Haagmans, G. A. Hamilton, A. L. Hartman, S. Herfst, S. J. F. Kaptein, W. B. Klimstra, I. Knezevic, P. R. Krause, J. H. Kuhn, R. L. Grand, M. G. Lewis, W.-C. Liu, P. Maisonnasse, A. K. McElroy, V. Munster, N. Oreshkova, A. L. Rasmussen, J. Rocha-Pereira, B. Rockx, E. Rodríguez, T. F. Rogers, F. J. Salguero, M. Schotsaert, K. J. Stittelaar, H. J. Thibaut, C.-T. Tseng, J. Vergara-Alert, M. Beer, T. Brasel, J. F. W. Chan, A. García-Sastre, J. Neyts, S. Perlman, D. S. Reed, J. A. Richt, C. J. Roy, J. Segalés, S. S. Vasan, A. M. Henao-Restrepo, D. H. Barouch, Animal models for COVID-19. *Nature* **586**, 509–515 (2020).
14. P. B. McCray, L. Pewe, C. Wohlford-Lenane, M. Hickey, L. Manzel, L. Shi, J. Netland, H. P. Jia, C. Halabi, C. D. Sigmund, D. K. Meyerholz, P. Kirby, D. C. Look, S. Perlman, Lethal infection of K18-hACE2 mice infected with severe acute respiratory syndrome coronavirus. *J. Virol.* **81**, 813–821 (2007).
15. Y.-H. Chow, H. O'Brodovich, J. Plumb, Y. Wen, K.-J. Sohn, Z. Lu, F. Zhang, G. L. Lukacs, A. K. Tanswell, C.-C. Hui, M. Buchwald, J. Hu, Development of an epithelium-specific expression cassette with human DNA regulatory elements for transgene expression in lung airways. *Proc. Natl. Acad. Sci. U.S.A.* **94**, 14695–14700 (1997).
16. R.-D. Jiang, M.-Q. Liu, Y. Chen, C. Shan, Y.-W. Zhou, X.-R. Shen, Q. Li, L. Zhang, Y. Zhu, H.-R. Si, Q. Wang, J. Min, X. Wang, W. Zhang, B. Li, H.-J. Zhang, R. S. Baric, P. Zhou, X.-L. Yang, Z.-L. Shi, Pathogenesis of SARS-CoV-2 in transgenic mice expressing human angiotensin-converting enzyme 2. *Cell* **182**, 50–58.e8 (2020).
17. S.-H. Sun, Q. Chen, H.-J. Gu, G. Yang, Y.-X. Wang, X.-Y. Huang, S.-S. Liu, N.-N. Zhang, X.-F. Li, R. Xiong, Y. Guo, Y.-Q. Deng, W.-J. Huang, Q. Liu, Q.-M. Liu, Y.-L. Shen, Y. Zhou, X. Yang, T.-Y. Zhao, C.-F. Fan, Y.-S. Zhou, C.-F. Qin, Y.-C. Wang, A mouse model of SARS-CoV-2 infection and pathogenesis. *Cell Host Microbe.* **28**, 124–133.e4 (2020).
18. E. S. Winkler, A. L. Bailey, N. M. Kafai, S. Nair, B. T. McCune, J. Yu, J. M. Fox, R. E. Chen, J. T. Earnest, S. P. Keeler, J. H. Ritter, L.-I. Kang, S. Dort, A. Robichaud, R. Head, M. J. Holtzman, M. S. Diamond, SARS-CoV-2 infection of human ACE2-transgenic mice causes severe lung inflammation and impaired function. *Nat. Immunol.* **21**, 1327–1335 (2020).
19. J. Zheng, L.-Y. R. Wong, K. Li, A. K. Verma, M. E. Ortiz, C. Wohlford-Lenane, M. R. Leidinger, C. M. Knudson, D. K. Meyerholz, P. B. McCray, S. Perlman, COVID-19 treatments and pathogenesis including anosmia in K18-hACE2 mice. *Nature* **589**, 603–607 (2021).
20. P. Kumari, H. A. Rothan, J. P. Natekar, S. Stone, H. Pathak, P. G. Strate, K. Arora, M. A. Brinton, M. Kumar, Neuroinvasion and encephalitis following intranasal inoculation of SARS-CoV-2 in K18-hACE2 mice. *Viruses* **13**, 132 (2021).
21. L. Zhou, S. K. Ayeh, V. Chidambaram, P. C. Karakousis, Modes of transmission of SARS-CoV-2 and evidence for preventive behavioral interventions. *BMC Infect. Dis.* **21**, 496 (2021).

22. R. J. Goody, C. C. Hoyt, K. L. Tyler, Reovirus infection of the CNS enhances iNOS expression in areas of virus-induced injury. *Exp. Neurol.* **195**, 379–390 (2005).
23. B. T. Bradley, H. Maioli, R. Johnston, I. Chaudhry, S. L. Fink, H. Xu, B. Najafian, G. Deutsch, J. M. Lacy, T. Williams, N. Yarid, D. A. Marshall, Histopathology and ultrastructural findings of fatal COVID-19 infections in Washington State: A case series. *Lancet* **396**, 320–332 (2020).
24. J. Kantonen, S. Mahzabin, M. I. Mäyränpää, O. Tynninen, A. Paetau, N. Andersson, A. Sajantila, O. Vapalahti, O. Carpén, E. Kekäläinen, A. Kantele, L. Myllykangas, Neuropathologic features of four autopsied COVID-19 patients. *Brain Pathol.* **30**, 1012–1016 (2020).
25. J. Meinhardt, J. Radke, C. Dittmayer, J. Franz, C. Thomas, R. Mothes, M. Laue, J. Schneider, S. Brünink, S. Greuel, M. Lehmann, O. Hassan, T. Aschman, E. Schumann, R. L. Chua, C. Conrad, R. Eils, W. Stenzel, M. Windgassen, L. Rößler, H.-H. Goebel, H. R. Gelderblom, H. Martin, A. Nitsche, W. J. Schulz-Schaeffer, S. Hakroush, M. S. Winkler, B. Tampe, F. Scheibe, P. Körtvélyessy, D. Reinhold, B. Siegmund, A. A. Kühl, S. Elezkurtaj, D. Horst, L. Oesterhelweg, M. Tsokos, B. Ingold-Heppner, C. Stadelmann, C. Drosten, V. M. Corman, H. Radbruch, F. L. Heppner, Olfactory transmucosal SARS-CoV-2 invasion as a port of central nervous system entry in individuals with COVID-19. *Nat. Neurosci.* **24**, 168–175 (2021).
26. R. R. Reichard, K. B. Kashani, N. A. Boire, E. Constantopoulos, Y. Guo, C. F. Lucchinetti, Neuropathology of COVID-19: A spectrum of vascular and acute disseminated encephalomyelitis (ADEM)-like pathology. *Acta Neuropathol.* **140**, 1–6 (2020).
27. G. E. Serrano, J. E. Walker, R. Arce, M. J. Glass, D. Vargas, L. I. Sue, A. J. Intorcia, C. M. Nelson, J. Oliver, J. Papa, A. Russell, K. E. Suszczewicz, C. I. Borja, C. Belden, D. Goldfarb, D. Shprecher, A. Atri, C. H. Adler, H. A. Shill, E. Driver-Dunckley, S. H. Mehta, B. Readhead, M. J. Huentelman, J. L. Peters, E. Alevritis, C. Bimi, J. P. Mizgerd, E. M. Reiman, T. J. Montine, M. Desforges, J. L. Zehnder, M. K. Sahoo, H. Zhang, D. Solis, B. A. Pinsky, M. Deture, D. W. Dickson, T. G. Beach, Mapping of SARS-CoV-2 brain invasion and histopathology in COVID-19 disease. *Medrxiv*, in press (2021), doi:10.1101/2021.02.15.21251511.
28. M. Khan, S.-J. Yoo, M. Clijsters, W. Backaert, A. Vanstapel, K. Speleman, C. Lietaer, S. Choi, T. D. Hether, L. Marcelis, A. Nam, L. Pan, J. W. Reeves, P. V. Bulck, H. Zhou, M. Bourgeois, Y. Debaveye, P. D. Munter, J. Gunst, M. Jorissen, K. Lagrou, N. Lorent, A. Neyrinck, M. Peetermans, D. R. Thal, C. Vandenbriele, J. Wauters, P. Mombaerts, L. V. Gerven, Visualizing in deceased COVID-19 patients how SARS-CoV-2 attacks the respiratory and olfactory mucosae but spares the olfactory bulb. *Cell* **184**, 5932–5949.e15 (2021).
29. Q. Ye, J. Zhou, Q. He, R.-T. Li, G. Yang, Y. Zhang, S.-J. Wu, Q. Chen, J.-H. Shi, R.-R. Zhang, H.-M. Zhu, H.-Y. Qiu, T. Zhang, Y.-Q. Deng, X.-F. Li, J.-F. Liu, P. Xu, X. Yang, C.-F. Qin, SARS-CoV-2 infection in the mouse olfactory system. *Cell Discov.* **7**, 49 (2021).
30. S. R. Leist, K. H. Dinnon, A. Schäfer, L. V. Tse, K. Okuda, Y. J. Hou, A. West, C. E. Edwards, W. Sanders, E. J. Fritch, K. L. Gully, T. Scobey, A. J. Brown, T. P. Sheahan, N. J. Moorman, R. C. Boucher, L. E. Gralinski, S. A. Montgomery, R. S. Baric, A mouse-adapted SARS-CoV-2 induces acute lung injury and mortality in standard laboratory mice. *Cell* **183**, 1070–1085.e12 (2020).
31. V. D. Menachery, L. E. Gralinski, R. S. Baric, M. T. Ferris, New metrics for evaluating viral respiratory pathogenesis. *PLOS ONE.* **10**, e0131451 (2015).
32. J. Bates, C. Irvin, V. Brusasco, J. Drazen, J. Fredberg, S. Loring, D. Eidelman, M. Ludwig, P. Macklem, J. Martin, J. Milic-Emili, Z. Hantos, R. Hyatt, S. Lai-Fook, A. Leff, J. Solway, K. Lutchen, B. Suki, W. Mitzner, P. Paré, N. Pride, P. Sly, The use and misuse of Penh in animal models of lung disease. *Am. J. Resp. Cell Mol.* **31**, 373–374 (2004).
33. L. K. A. Lundblad, C. G. Irvin, Z. Hantos, P. Sly, W. Mitzner, J. H. T. Bates, Penh is not a measure of airway resistance! *Eur. Respir. J.* **30**, 805–805 (2007).
34. M. Lomask, Further exploration of the Penh parameter. *Exp. Toxicol. Pathol.* **57**, 13–20 (2006).
35. S. F. Lax, K. Skok, P. Zechner, H. H. Kessler, N. Kaufmann, C. Koelblinger, K. Vander, U. Bargfrieder, M. Trauner, Pulmonary arterial thrombosis in COVID-19 with fatal outcome: Results from a prospective, single-center, Clinicopathologic Case Series. *Ann. Intern. Med.* **173**, 350–361 (2020).
36. S. E. Fox, A. Akmatbekov, J. L. Harbert, G. Li, J. Q. Brown, R. S. V. Heide, Pulmonary and cardiac pathology in African American patients with COVID-19: An autopsy series from New Orleans. *Lancet Respir. Med.* **8**, 681–686 (2020).
37. M. Dolhnikoff, A. N. Duarte-Neto, R. A. A. Monteiro, L. F. F. Silva, E. P. Oliveira, P. H. N. Saldiva, T. Mauad, E. M. Negri, Pathological evidence of pulmonary thrombotic phenomena in severe COVID-19. *J. Thromb. Haemost.* **18**, 1517–1519 (2020).
38. A. E. Mast, A. S. Wolberg, D. Gailani, M. R. Garvin, C. Alvarez, J. I. Miller, B. Aronow, D. Jacobson, SARS-CoV-2 suppresses anticoagulant and fibrinolytic gene expression in the lung. *eLife* **10**, e64330 (2021).
39. B. K. Manne, F. Denorme, E. A. Middleton, I. Portier, J. W. Rowley, C. Stubben, A. C. Petrey, N. D. Tolley, L. Guo, M. Cody, A. S. Weyrich, C. C. Yost, M. T. Rondina, R. A. Campbell, Platelet gene expression and function in patients with COVID-19. *Blood* **136**, 1317–1329 (2020).
40. T. M. Delorey, C. G. K. Ziegler, G. Heimberg, R. Normand, Y. Yang, Å. Segerstolpe, D. Abbondanza, S. J. Fleming, A. Subramanian, D. T. Montoro, K. A. Jagadeesh, K. K. Dey, P. Sen, M. Slyper, Y. H. Pita-Juárez, D. Phillips, J. Biermann, Z. Bloom-Ackermann, N. Barkas, A. Ganna, J. Gomez, J. C. Melms, I. Katsyv, E. Normandin, P. Naderi, Y. V. Popov, S. S. Raju, S. Niezen, L. T.-Y. Tsai, K. J. Siddle, M. Sud, V. M. Tran, S. K. Vellarikkal, Y. Wang, L. Amir-Zilberstein, D. S. Atri, J. Beechem, O. R. Brook, J. Chen, P. Divakar, P. Dorceus, J. M. Engreitz, A. Essene, D. M. Fitzgerald, R. Fropf, S. Gazal, J. Gould, J. Grzyb, T. Harvey, J. Hecht, T. Hether, J. Jané-Valbuena, M. Leney-Greene, H. Ma, C. McCabe, D. E. McLoughlin, E. M. Miller, C. Muus, M. Niemi, R. Padera, L. Pan, D. Pant, C. Pe'er, J. Pfiffner-Borges, C. J. Pinto, J. Plaisted, J. Reeves, M. Ross, M. Rudy, E. H. Rueckert, M. Siciliano, A. Sturm, E. Todres, A. Waghray, S. Warren, S. Zhang, D. R. Zollinger, L. Cosimi, R. M. Gupta, N. Hacohen, H. Hibshoosh, W. Hide, A. L. Price, J. Rajagopal, P. R. Tata, S. Riedel, G. Szabo, T. L. Tickle, P. T. Ellinor, D. Hung, P. C. Sabeti, R. Novak, R. Rogers, D. E. Ingber, Z. G. Jiang, D. Juric, M. Babadi, S. L. Farhi, B. Izar, J. R. Stone, I. S. Vlachos, I. H. Solomon, O. Ashenberg, C. B. M. Porter, B. Li, A. K. Shalek, A.-C. Villani, O. Rozenblatt-Rosen, A. Regev, COVID-19 tissue atlases reveal SARS-CoV-2 pathology and cellular targets. *Nature* **595**, 107–113 (2021).
41. D. Blanco-Melo, B. E. Nilsson-Payant, W.-C. Liu, S. Uhl, D. Hoagland, R. Møller, T. X. Jordan, K. Oishi, M. Panis, D. Sachs, T. T. Wang, R. E. Schwartz, J. K. Lim, R. A. Albrecht, B. R. tenOever, Imbalanced host response to SARS-CoV-2 drives development of COVID-19. *Cell* **181**, 1036–1045.e9 (2020).
42. R. Karki, B. R. Sharma, S. Tuladhar, E. P. Williams, L. Zalduondo, P. Samir, M. Zheng, B. Sundaram, B. Banoth, R. K. S. Malireddi, P. Schreiner, G. Neale, P. Vogel, R. Webby, C. B. Jonsson, T.-D. Kanneganti, Synergism of TNF-α and IFN-γ triggers inflammatory cell death, tissue damage, and mortality in SARS-CoV-2 infection and cytokine shock syndromes. *Cell* **184**, 149–168.e17 (2021).
43. Z. Zhuang, X. Lai, J. Sun, Z. Chen, Z. Zhang, J. Dai, D. Liu, Y. Li, F. Li, Y. Wang, A. Zhu, J. Wang, W. Yang, J. Huang, X. Li, L. Hu, L. Wen, J. Zhuo, Y. Zhang, D. Chen, S. Li, S. Huang, Y. Shi, K. Zheng, N. Zhong, J. Zhao, D. Zhou, J. Zhao, Mapping and role of T cell response in SARS-CoV-2–infected mice. *J. Exp. Med.* **218**, 20202187 (2021).
44. C. H. Sudre, A. Keshet, M. S. Graham, A. D. Joshi, S. Shilo, H. Rossman, B. Murray, E. Molteni, K. Klaser, L. D. Canas, M. Antonelli, L. H. Nguyen, D. A. Drew, M. Modat, J. C. Pujol, S. Ganesh, J. Wolf, T. Meir, A. T. Chan, C. J. Steves, T. D. Spector, J. S. Brownstein, E. Segal, S. Ourselin, C. M. Astley, Anosmia, ageusia, and other COVID-19-like symptoms in association with a positive SARS-CoV-2 test, across six national digital surveillance platforms: An observational study. *Lancet Digital Heal.* **3**, e577–e586 (2021).
45. K. Bilinska, P. Jakubowska, C. S. V. Bartheld, R. Butowt, Expression of the SARS-CoV-2 entry proteins, ACE2 and TMPRSS2, in cells of the olfactory epithelium: Identification of cell types and trends with age. *ACS Chem. Nerosci.* **11**, 1555–1562 (2020).
46. D. H. Brann, T. Tsukahara, C. Weinreb, M. Lipovsek, K. V. den Berge, B. Gong, R. Chance, I. C. Macaulay, H.-J. Chou, R. B. Fletcher, D. Das, K. Street, H. R. de Bezieux, Y.-G. Choi, D. Risso, S. Dudoit, E. Purdom, J. Mill, R. A. Hachem, H. Matsunami, D. W. Logan, B. J. Goldstein, M. S. Grubb, J. Ngai, S. R. Datta, Non-neuronal expression of SARS-CoV-2 entry genes in the olfactory system suggests mechanisms underlying COVID-19-associated anosmia. *Sci. Adv.* **6**, eabc5801 (2020).
47. L. Fodoulian, J. Tuberosa, D. Rossier, M. Boillat, C. Kan, V. Pauli, K. Egervari, J. A. Lobrinus, B. N. Landis, A. Carleton, I. Rodriguez, SARS-CoV-2 receptors and entry genes are expressed in the human olfactory neuroepithelium and brain. *iScience* **23**, 101839 (2020).
48. A. Torabi, E. Mohammadbagheri, N. A. Dilmaghani, A.-H. Bayat, M. Fathi, K. Vakili, R. Alizadeh, O. Rezaeimirghaed, M. Hajiesmaeili, M. Ramezani, L. Simani, A. Aliaghaei, Proinflammatory cytokines in the olfactory mucosa result in COVID-19 induced anosmia. *ACS Chem. Neurosci.* **11**, 1909–1913 (2020).
49. A. J. Zhang, A. C.-Y. Lee, H. Chu, J. F.-W. Chan, Z. Fan, C. Li, F. Liu, Y. Chen, S. Yuan, V. K.-M. Poon, C. C.-S. Chan, J.-P. Cai, K. L.-K. Wu, S. Sridhar, Y.-S. Chan, K.-Y. Yuen, SARS-CoV-2 infects and damages the mature and immature olfactory sensory neurons of hamsters. *Clin. Infect. Dis.* **73**, e503–e512 (2021).
50. B. Bryche, A. S. Albin, S. Murri, S. Lacôte, C. Pulido, M. A. Gouilh, S. Lesellier, A. Servat, M. Wasniewski, E. Picard-Meyer, E. Monchatre-Leroy, R. Volmer, O. Rampin, R. L. Goffic, P. Marianneau, N. Meunier, Massive transient damage of the olfactory epithelium associated with infection of sustentacular cells by SARS-CoV-2 in golden Syrian hamsters. *Brain Behav. Immun.* **89**, 579–586 (2020).
51. M. Klingenstein, S. Klingenstein, P. H. Neckel, A. F. Mack, A. P. Wagner, A. Kleger, S. Liebau, A. Milazzo, Evidence of SARS-CoV2 entry protein ACE2 in the human nose and olfactory bulb. *Cells Tissues Organs* **209**, 155–164 (2020).
52. C. Meisel, J. M. Schwab, K. Prass, A. Meisel, U. Dirnagl, Central nervous system injury-induced immune deficiency syndrome. *Nat. Rev. Neurosci.* **6**, 775–786 (2005).
53. I. Boukhatem, S. Fleury, M. Welman, J. L. Blanc, C. Thys, K. Freson, M. G. Best, T. Würdinger, B. G. Allen, M. Lordkipanidzé, The brain-derived neurotrophic factor prompts platelet aggregation and secretion. *Blood Adv.* **5**, 3568–3580 (2021).
54. J. H. Smith, T. Nagy, J. Barber, P. Brooks, S. M. Tompkins, R. A. Tripp, Aerosol inoculation with a sub-lethal influenza virus leads to exacerbated morbidity and pulmonary disease pathogenesis. *Viral Immunol.* **24**, 131–142 (2011).

55. R. Huang, I. Grishagin, Y. Wang, T. Zhao, J. Greene, J. C. Obenauer, D. Ngan, D.-T. Nguyen, R. Guha, A. Jadhav, N. Southall, A. Simeonov, C. P. Austin, The NCATS BioPlanet – An integrated platform for exploring the universe of cellular signaling pathways for toxicology, systems biology, and chemical genomics. *Front. Pharmacol.* **10**, 445 (2019).
56. M. Iannacone, G. Sitia, M. Isogawa, J. K. Whitmire, P. Marchese, F. V. Chisari, Z. M. Ruggeri, L. G. Guidotti, Platelets prevent IFN-α/β-induced lethal hemorrhage promoting CTL-dependent clearance of lymphocytic choriomeningitis virus. *Proc. Natl. Acad. Sci. U.S.A.* **105**, 629–634 (2008).
57. A. P. Béréchet, G. D. Simone, P. D. Lucia, F. Cilenti, G. Barbiera, N. L. Bert, V. Fumagalli, E. Lusito, F. Moalli, V. Bianchessi, F. Andreata, P. Zordan, E. Bono, L. Giustini, W. V. Bonilla, C. Bleriot, K. Kunasegaran, G. Gonzalez-Aseguinolaza, D. D. Pinschewer, P. T. F. Kennedy, L. Naldini, M. Kuka, F. Ginhoux, A. Cantore, A. Bertoletti, R. Ostuni, L. G. Guidotti, M. Iannacone, Dynamics and genomic landscape of $CD8^+$ T cells undergoing hepatic priming. *Nature* **574**, 200–205 (2019).
58. S. Picelli, O. R. Faridani, Å. K. Björklund, G. Winberg, S. Sagasser, R. Sandberg, Full-length RNA-seq from single cells using Smart-seq2. *Nat. Protoc.* **9**, 171–181 (2014).
59. A. Dobin, C. A. Davis, F. Schlesinger, J. Drenkow, C. Zaleski, S. Jha, P. Batut, M. Chaisson, T. R. Gingeras, STAR: Ultrafast universal RNA-seq aligner. *Bioinformatics* **29**, 15–21 (2013).
60. Y. Liao, G. K. Smyth, W. Shi, The R package Rsubread is easier, faster, cheaper and better for alignment and quantification of RNA sequencing reads. *Nucleic Acids Res.* **47**, e47 (2019).
61. M. D. Robinson, A. Oshlack, A scaling normalization method for differential expression analysis of RNA-seq data. *Genome Biol.* **11**, R25 (2010).
62. C. W. Law, Y. Chen, W. Shi, G. K. Smyth, voom: Precision weights unlock linear model analysis tools for RNA-seq read counts. *Genome Biol.* **15**, R29 (2014).
63. M. E. Ritchie, B. Phipson, D. Wu, Y. Hu, C. W. Law, W. Shi, G. K. Smyth, *limma* powers differential expression analyses for RNA-sequencing and microarray studies. *Nucleic Acids Res.* **43**, e47 (2015).
64. A. Subramanian, P. Tamayo, V. K. Mootha, S. Mukherjee, B. L. Ebert, M. A. Gillette, A. Paulovich, S. L. Pomeroy, T. R. Golub, E. S. Lander, J. P. Mesirov, Gene set enrichment analysis: A knowledge-based approach for interpreting genome-wide expression profiles. *Proc. Natl. Acad. Sci. U.S.A.* **102**, 15545–15550 (2005).
65. L. G. Guidotti, D. Inverso, L. Sironi, P. Di Lucia, J. Fioravanti, L. Ganzer, A. Fiocchi, M. Vacca, R. Aiolfi, S. Sammicheli, M. Mainetti, T. Cataudella, A. Raimondi, G. Gonzalez-Aseguinolaza, U. Protzer, Z. M. Ruggeri, F. V. Chisari, M. Isogawa, G. Sitia, M. Iannacone, Immunosurveillance of the liver by intravascular effector CD8+ T cells. *Cell* **161**, 486–500 (2015).

Acknowledgments: We thank M. Freschi, M. Raso, A. Fiocchi, M. Genua, R. Ostuni, and S. Grassi for technical support; M. Silva for secretarial assistance; and the members of the Iannacone laboratory for helpful discussions. Flow cytometry was carried out at FRACTAL, a flow cytometry resource and advanced cytometry technical applications laboratory established by the San Raffaele Scientific Institute. Confocal immunofluorescence histology was carried out at Alembic, an advanced microscopy laboratory established by the San Raffaele Scientific Institute and the Vita-Salute San Raffaele University. We would like to acknowledge the PhD program in Basic and Applied Immunology and Oncology at Vita-Salute San Raffaele University, as D.M. and E.S. conducted this study as partial fulfillment of their PhD in Molecular Medicine within that program. **Funding:** M.I. is supported by the European Research Council (ERC) Consolidator Grant 725038, ERC Proof of Concept Grant 957502, Italian Association for Cancer Research (AIRC) Grants 19891 and 22737, Italian Ministry of Health Grants RF-2018-12365801 and COVID-2020-12371617, Lombardy Foundation for Biomedical Research (FRRB) Grant 2015-0010, the European Molecular Biology Organization Young Investigator Program, and Funded Research Agreements from Gilead Sciences, GSK Vaccines, Takis Biotech, and Toscana Life Sciences. L.G.G. is supported by the Italian Association for Cancer Research (AIRC) Grant 22737; Lombardy Open Innovation Grant 229452; PRIN Grant 2017MPCWPY from the Italian Ministry of Education, University and Research; Funded Research Agreements from Gilead Sciences, Avalia Therapeutics, and CNCCS SCARL and donations from FONDAZIONE SAME and FONDAZIONE PROSSIMO MIO for COVID-19–related research. M.K. is supported by the Italian Ministry of Education, University and Research grants SIR-RBSI14BAO5 and PRIN-2017ZXT5WR. **Author contributions:** Conceptualization, V.F., L.G.G., and M.I. Investigation: V.F., M.R., D.M., P.D.L., C.L., E.S., M.G., E.B., L.G., C.P., M.M., A.S., and J.M.G.-M. Resources: L.D., L.M., S.D., and R.D.F. Formal analysis: V.F., M.R., D.M., E.S., V.B., P.D'A., and M.K. Writing: V.F., M.K., L.G.G., and M.I. with input from all authors. Visualization: V.F. Funding acquisition: L.G.G. and M.I. Project supervision: M.I. **Competing interests:** M.I. participates in advisory boards/consultancies for Gilead Sciences, Roche, Third Rock Ventures, Amgen, Allovir, Asher Bio, and ENYO Pharma. L.G.G. is a member of the board of directors at Genenta Science and Epsilon Bio and participates in advisory boards/consultancies for Gilead Sciences, Roche, and Arbutus Biopharma. **Data and materials availability:** The RNA-seq data reported in this study have been deposited in the database Gene Expression Omnibus (accession number GSE184657).

Submitted 19 August 2021
Accepted 15 November 2021
Published First Release 23 November 2021
Final Published 28 January 2022
10.1126/sciimmunol.abl9929